JACS
JOURNAL OF THE AMERICAN CHEMICAL SOCIETY

Article

pubs.acs.org/JACS

Metal–Semiconductor Heteronanocrystals with Desired Configurations for Plasmonic Photocatalysis

Jong Wook Hong,[†,‡] Dae Han Wi,[†] Su-Un Lee,[†] and Sang Woo Han*[,†]

[†]Center for Nanotectonics, Department of Chemistry and KI for the NanoCentury, KAIST, Daejeon 34141, Korea
[‡]Department of Chemistry, University of Ulsan, Ulsan 44610, Korea

Supporting Information

ABSTRACT: Precise control over the topology of plasmonic metal–semiconductor heteronanostructures is essential for fully harnessing their plasmonic function and hence for designing innovative solar energy conversion platforms. Here, we present a rational synthesis strategy for the realization of plasmonic metal–semiconductor heteronanocrystals with intended configurations through the site-selective overgrowth of semiconductor Cu_2O on desired sites of anisotropic Au nanocrystals. Both the exploitation of structural characteristics of Au nanocrystals and the selective stabilization of their surfaces are keys to the construction of heteronanocrystals with a specific configuration. Our approach can provide an opportunity to precisely explore the link between the solar energy conversion efficiency and the structure of heteronanocrystals as well as to obtain important insights into the underpinning mechanism. Heteronanocrystals produced by Cu_2O overgrowth preferentially on the multiple high-curvature sites of Au nanocrystals exhibited prominent photocatalytic hydrogen production activity due to efficient charge separation by strong plasmon excitation at the Au–Cu_2O interface and subsequent sustainable hot electron transfer from Au to Cu_2O.

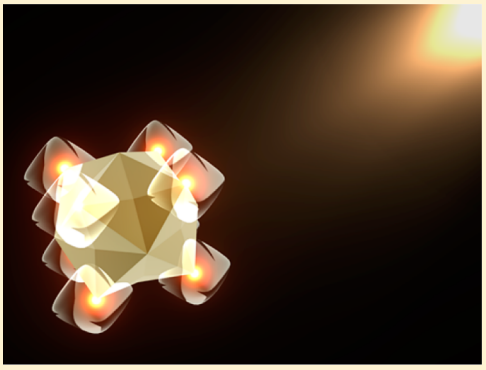

INTRODUCTION

Recently, substantial endeavors have been devoted to synthesizing heteronanocrystals (HNCs) with the combination of plasmonic metal NCs and semiconductors because they have shown excellent performance in many photocatalytic reactions, such as hydrogen production, as compared to their semiconductor counterparts.[1−8] The enhanced efficiency of solar energy conversion of HNCs is attributed to an increase in the rate of charge carrier generation in the constituent semiconductor due to the transfer of the plasmon energy of metal NC to the semiconductor. The plasmon energy of the metal NC associated with its surface plasmon resonance (SPR) can be transferred via either an SPR-induced hot electron transfer (HET) process, where SPR-induced hot electrons in the plasmonic metal NC are injected into the conduction band (CB) of the semiconductor,[6,9] or an electromagnetic (EM) field-mediated plasmon energy transfer process (EMT), such as plasmon-induced resonance energy transfer, during which the radiative or nonradiative relaxation of SPR of the metal NC mediates the plasmon energy transfer.[10,11] Despite enormous advances in this field, both the development of a rational synthetic strategy that can enable precise control over the structure of HNCs and the elucidation of the underpinning mechanism of plasmon energy transfer along with the structural characteristics of HNCs are still imperative to fully exploit the plasmonic function of the metal NC domain in HNCs and thus to devise innovative solar energy conversion platforms.

With regard to the development of a new design principle of HNCs with high solar energy conversion efficiency, it should be considered that the SPR properties of plasmonic metal NCs are highly dependent on their morphologies.[12] In this context, it is noteworthy that plasmon energy is typically concentrated at sites of high curvature, such as vertices, edges, and sharp branches of plasmonic metal NCs.[13−15] As such, the integration of plasmonic metal NCs with a large number of high-curvature sites and semiconductors will boost the efficiency of light harvesting. Besides the morphology of plasmonic metal NCs, the solar energy conversion efficiency of plasmonic metal–semiconductor HNCs is also sensitive to the manner of coupling between metal NCs and the semiconductor. For instance, HNCs with Janus and dumbbell-like structures formed from the anisotropic overgrowth of the semiconductor onto plasmonic metal NCs exhibited enhanced photocatalytic performance compared to that of homogeneous core–shell HNCs, because a strong SPR is localized at the interconnecting junction between plasmonic metals and semiconductors.[16−18] Furthermore, the exposed surfaces of both the metal and semiconductor domains of anisotropic HNCs can facilitate charge exchange between charge carriers in HNCs and their reaction partners.[19,20] Taken together, anisotropic HNCs generated by the selective growth of a semiconductor on multiple high-curvature sites of plasmonic NCs might hold

Received: October 1, 2016
Published: November 14, 2016

DOI: 10.1021/jacs.6b10288
J. Am. Chem. Soc. 2016, 138, 15766−15773

great potential to achieve excellent photocatalytic performance. However, due to the complexity of the coupling of a semiconductor at desired sites of plasmonic NCs, the realization of such HNCs has rarely been reported.

Herein, we report a novel synthetic approach for the site-selective growth of a semiconductor on desired sites of anisotropic plasmonic metal NCs. As a plasmonic NC platform for fabricating HNCs, high-index-faceted NCs are very promising due to their high density of high-curvature sites.[14,15,21,22] In this regard, we chose hexoctahedral (HOH) Au NCs enclosed by 48 triangular high-index {321} facets[22] as a plasmonic NC component (Figure S1), which have highly anisotropic structural characteristics imparted by a high density of vertices with distinctively different curvatures. Cuprous oxide (Cu_2O), a well-known p-type semiconductor with a direct band gap of around 2 eV,[23] was chosen as the semiconductor component. Through exploitation of the inherent structural features of the HOH Au NCs, the growth mode of Cu_2O on the HOH Au NCs could be manipulated with the assistance of relevant stabilizing agents. As a consequence, HNCs with explicitly different coupling manners between the HOH Au NCs and Cu_2O were selectively generated (Figure 1a): (1) Au_{vertex}−Cu_2O HNCs formed by the overgrowth of Cu_2O exclusively on the 8 vertices of the HOH Au NCs pointing toward the <111> direction (vertices$_{<111>}$, blue circles in the structural model of the HOH Au NC shown in Figure 1a), (2) $Au_{vertex\text{-}exp}$−Cu_2O HNCs formed by the growth of Cu_2O on the HOH Au NCs apart from the regions of the vertices$_{<111>}$, and (3) Au_{HOH}@Cu_2O HNCs formed by the isotropic growth of Cu_2O on the entire surface of the HOH Au NCs. Our approach, which can enable fine control over the structure of HNCs, could allow us to unequivocally elucidate the link between the solar energy conversion efficiency and the coupling manner of HNCs and facilitate studying the underlying mechanism of plasmon energy transfer in the course of photocatalysis. Apparently, the prepared HNCs exhibited distinctly different visible-light photocatalytic activities for hydrogen production. Among the different HNCs, the Au_{vertex}−Cu_2O HNCs generated by the selective overgrowth of Cu_2O on multiple high-curvature sites of the HOH Au NCs showed the most promoted photocatalytic activity, which is in line with our above-mentioned inference. This pronounced solar-to-fuel conversion efficiency of the Au_{vertex}−Cu_2O HNCs can be attributed to the plasmon energy transfer enhancement, which is predominantly due to the HET mechanism, as confirmed by a series of control experiments and finite-difference time domain (FDTD) simulations.

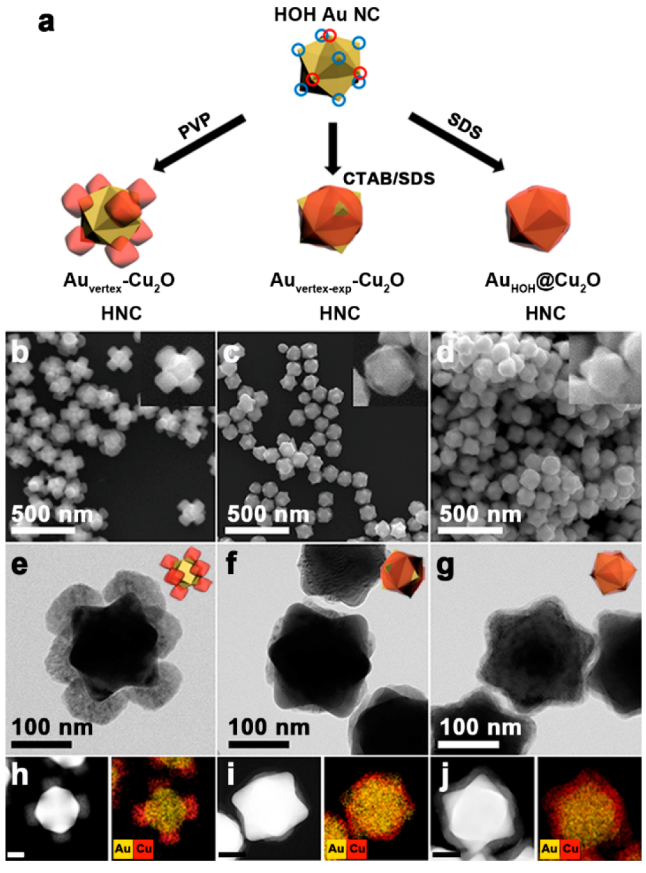

Figure 1. (a) Schematic illustration of the formation of Au−Cu_2O HNCs with different growth modes of Cu_2O. Blue and red circles indicate the vertices of HOH Au NC pointing toward the <111> and <100> directions, respectively. SEM (b−d), TEM (e−g), and HAADF-STEM and corresponding HAADF-STEM-EDS elemental mapping images (h−j) of Au_{vertex}−Cu_2O (b, e, and h), $Au_{vertex\text{-}exp}$−Cu_2O (c, f, and i), and Au_{HOH}@Cu_2O (d, g, and j) HNCs. The scale bars in h−j indicate 50 nm.

RESULTS AND DISCUSSION

Synthesis and Characterization of HNCs. HNCs with different coupling manners between the HOH Au NC and Cu_2O entities were synthesized via the growth of Cu_2O on the preformed HOH Au NCs with an average size of 130 ± 9 nm (Figure S1), which were prepared by following the reported procedure,[22] in the presence of poly(vinylpyrrolidone) (PVP), a cetyltrimethylammonium bromide (CTAB)/sodium dodecyl sulfate (SDS) binary mixture, and SDS for the cases of Au_{vertex}−Cu_2O, $Au_{vertex\text{-}exp}$−Cu_2O, and Au_{HOH}@Cu_2O HNCs, respectively (Figure 1a). See the Supporting Information for synthesis details. Figure 1b shows a typical scanning electron microscopy (SEM) image of the prepared Au_{vertex}−Cu_2O HNCs, revealing the formation of uniform HNCs by the selective overgrowth of Cu_2O on the vertices of the HOH Au NCs in the presence of PVP. The low-magnification SEM image of the sample further demonstrates the high-yield (>95%) production of Au_{vertex}−Cu_2O HNCs (Figure S2a). The average size of the Cu_2O domains grown on the vertices of the HOH Au NCs was 90 ± 9 nm. The high-magnification SEM images of the HNCs viewed along different directions closely match the corresponding three-dimensional geometric models of the HNC with the same orientations (Figure S2b,c), indicating that Cu_2O was deposited preferentially on the 8 vertices$_{<111>}$. The transmission electron microscopy (TEM) and high-angle annular dark-field scanning TEM-energy dispersive X-ray spectroscopy (HAADF-STEM-EDS) measurements on a single Au_{vertex}−Cu_2O HNC further show that Cu_2O indeed formed exclusively at the sharp 8 vertices$_{<111>}$ of the HOH Au NCs, and there was no deposition of Cu_2O at the other regions of the HOH Au NCs (Figure 1e,h). We performed additional selected-area HAADF-STEM-EDS-elemental analyses for the Au_{vertex}−Cu_2O HNC to check the possibility of Cu_2O growth in other regions apart from the vertices$_{<111>}$ (Figure 2a−d). In the central region of the HNC, only Au signal was detected (Figure 2c), whereas both Au and Cu signals were observed throughout the entire region of the HNC (Figure 2d), clearly indicating the site-selective growth of Cu_2O on the HOH Au NCs.

DOI: 10.1021/jacs.6b10288
J. Am. Chem. Soc. 2016, 138, 15766−15773

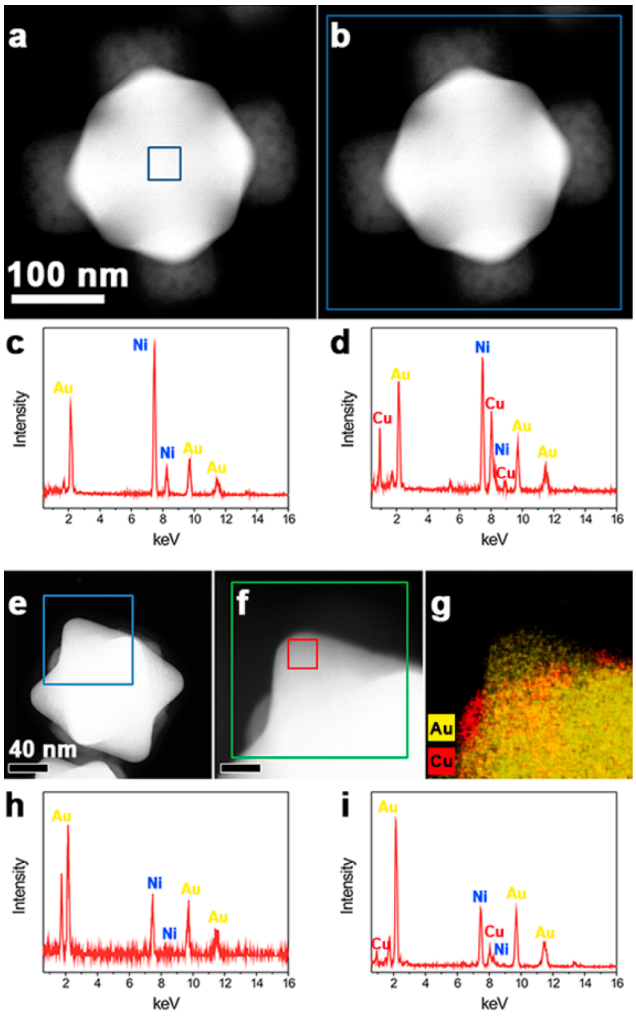

Figure 2. HAADF-STEM images (a and b) and corresponding EDS elemental analysis data (c and d) for the central (a and c) and entire region (b and d) of Au_{vertex}−Cu_2O HNC. (e) HAADF-STEM image of single $Au_{vertex\text{-}exp}$−Cu_2O HNC. High-magnification HAADF-STEM image (f) and corresponding HAADF-STEM-EDS elemental mapping image (g) of blue-square region in e. EDS elemental analysis data for red-square (h) and green-square (i) regions in f. The scale bar in f indicates 20 nm. Ni peaks in EDS data originated from Ni grids used in TEM measurements.

Interestingly, unlike the case of the Au_{vertex}−Cu_2O HNCs, the growth of Cu_2O was observed on the entire surface of the HOH Au NCs apart from their 8 $vertices_{<111>}$ in the case of the $Au_{vertex\text{-}exp}$−Cu_2O HNCs, which were prepared using the CTAB/SDS binary mixture instead of PVP as a stabilizing agent under otherwise similar synthesis conditions to those employed in the preparation of the Au_{vertex}−Cu_2O HNCs (Figure 1c,f,i). The average thickness of Cu_2O layers grown on the HOH Au NCs was 15 nm. High-magnification HAADF-STEM-EDS-elemental analyses for the $vertices_{<111>}$ region of the $Au_{vertex\text{-}exp}$−Cu_2O HNC explicitly verified that their $vertices_{<111>}$ were exposed (Figure 2e−i). In contrast, when an analogue synthesis was performed in the presence of SDS, Au_{HOH}@Cu_2O core−shell HNCs with an average Cu_2O shell thickness of 10 nm were formed by the isotropic growth of Cu_2O on the entire surface of the HOH Au NCs (Figure 1d,g,j).

The X-ray diffraction (XRD) patterns of all the HNCs exhibited typical diffraction peaks corresponding to the reflections from the face-centered cubic structure of Au and the cuprite structure of Cu_2O, indicating the crystalline nature of the prepared HNCs (Figure S3a,c,e). In addition, X-ray photoelectron spectroscopy (XPS) measurements on the Cu 2p core level of the HNCs verified that the Cu in the HNCs was almost in the Cu(I) state (Figure S3b,d,f).

Control over the Configuration of HNCs. The experimental results indicate that the proper use of a stabilizer is the key synthetic lever for the formation of HNCs with a desired coupling manner between metal and semiconductor entities. This can be attributed to the difference between the stabilization habits of the stabilizers employed in the synthesis. The HOH Au NCs, which were used as seeds for the formation of the HNCs, have multiple sharp vertices. Among them, the 8 $vertices_{<111>}$ have a higher curvature than the 6 vertices pointing toward the <100> direction ($vertices_{<100>}$, red circles in the structural model of the HOH Au NC shown in Figure 1a). Given that polymer or bilayer-forming surfactant molecules generally exhibit sparse coverage at high-curvature sites of NCs compared to that at low-curvature sites,[24−26] the $vertices_{<111>}$ can act as more efficient nucleation sites for the growth of Cu_2O compared to the $vertices_{<100>}$. Indeed, Cu_2O was preferentially formed at the $vertices_{<111>}$ of the HOH Au NCs in the presence of PVP, resulting in the production of the Au_{vertex}−Cu_2O HNCs. Similarly, HNCs with a coupling mode of Cu_2O identical to that of the Au_{vertex}−Cu_2O HNCs could also be prepared by using a bilayer-forming surfactant, such as CTAB, as a stabilizer instead of PVP (Figure S4).

To further verify the effect of the curvature of surface sites on Au NCs on the growth mode of Cu_2O, Au−Cu_2O HNCs were prepared by using other high-index-faceted Au NC seeds with different surface curvatures, such as Au truncated ditetragonal prisms (Au TDPs, Figure 3a,b)[27] and Au concave nanocubes (Au CNCs, Figure 4a,b),[28] while other experimental conditions

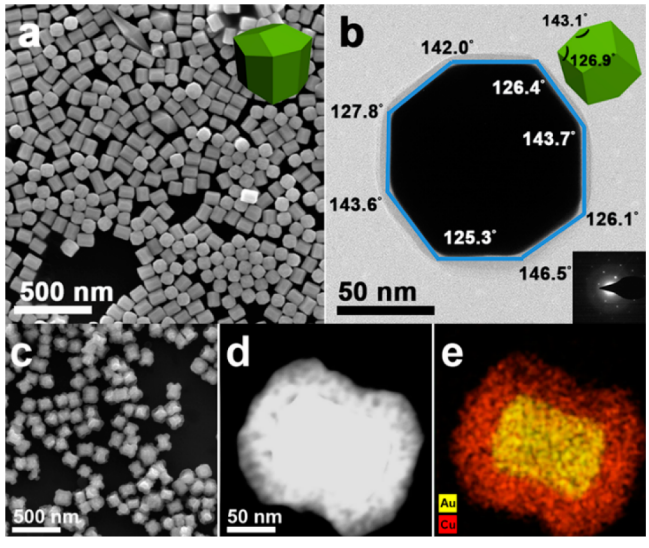

Figure 3. (a) SEM image and (inset) corresponding structural model of the Au TDPs. (b) TEM image and (bottom-right inset) corresponding selected area electron diffraction (SAED) pattern of the Au TDP viewed along the <110> direction. Structural model of the Au TDP with the same orientation is also shown in top-right inset. (c) SEM, (d) HAADF-STEM, and (e) HAADF-STEM-EDS elemental mapping images of the Au_{TDP}@Cu_2O core−shell HNCs.

DOI: 10.1021/jacs.6b10288
J. Am. Chem. Soc. 2016, 138, 15766−15773

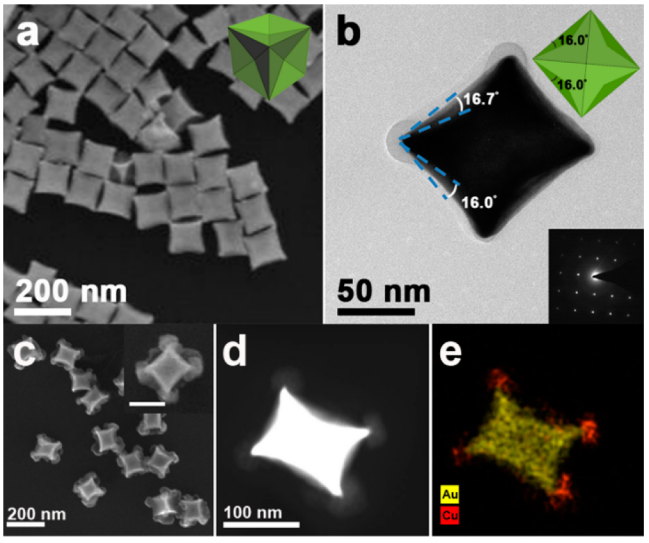

Figure 4. (a) SEM image and (inset) corresponding structural model of the Au CNCs. (b) TEM image and (bottom-right inset) corresponding SAED pattern of the Au CNC viewed along the <110> direction. Structural model of the Au CNC with the same orientation is also shown in top-right inset. (c) SEM and (inset) high-magnification SEM (scale bar = 100 nm), (d) HAADF-STEM, and (e) HAADF-STEM-EDS elemental mapping images of the Au_{CNC}−Cu_2O HNCs.

were retained. The exposed facets of the Au TDPs and Au CNCs were indexed, respectively, as {310} and {730} by comparing the measured and calculated angles between adjacent edge-on facets (Figures 3b and 4b). Au CNCs have many high-curvature sites like HOH Au NCs, whereas the vertices and edges of Au TDPs have relatively lower curvatures compared to those of HOH Au NCs and Au CNCs. Interestingly, Cu_2O was deposited over the whole surface of the Au TDPs (Figure 3c−e), while the formation of Cu_2O took place on the sharp vertices and edges of the Au CNCs (Figure 4c−e). These results clearly show the importance of the high-curvature sites of Au NCs for the realization of the site-selective overgrowth of Cu_2O. Noticeably, the present approach is also applicable to the selective overgrowth of secondary metals on the surfaces of Au NCs. For instance, Au_{vertex}−Ag HNCs were yielded through the overgrowth of Ag preferentially at the $vertices_{<111>}$ of the HOH Au NCs in the presence of PVP (Figure S5). On the contrary, when PVP stabilizer was substituted by SDS, which has been used to drive homogeneous overgrowth of metal oxides on Au NCs as it forms random assembly around NC surfaces due to its weak protecting ability,[8,29−31] Au_{HOH}@Cu_2O HNCs with complete shells of Cu_2O were produced instead of Au_{vertex}−Cu_2O HNCs.

For the formation of $Au_{vertex\text{-}exp}$−Cu_2O HNCs, we employed a CTAB/SDS binary stabilizer system in the synthesis. Due to the electrostatic interaction between the oppositely charged head groups of CTAB ($-N^+(CH_3)_3$) and SDS ($-OSO_3^-$) mediated by the interaction between their tail groups, CTAB/SDS binary mixtures readily form mixed micelles in aqueous solution, which are more stable than their pure counterparts.[32,33] As the CTAB/SDS binary stabilizer in the form of mixed micelle would prefer to adsorb on the high-curvature sites of HOH Au NCs, such as the $vertices_{<111>}$, due to their high surface energy,[31] the nucleation/growth of Cu_2O could proceed on other surface sites of HOH Au NCs rather than on the $vertices_{<111>}$ in the presence of the CTAB/SDS binary stabilizer, resulting in the formation of $Au_{vertex\text{-}exp}$−Cu_2O HNCs. To corroborate the selective stabilization action of the CTAB/SDS binary stabilizer, we conducted a systematic study on the influence of the curvature of surface sites of Au NCs on the growth mode of Cu_2O using Au nanorods with different curvatures in their tips as templates, while other synthesis conditions were maintained (Figure 5). For convenience, Au

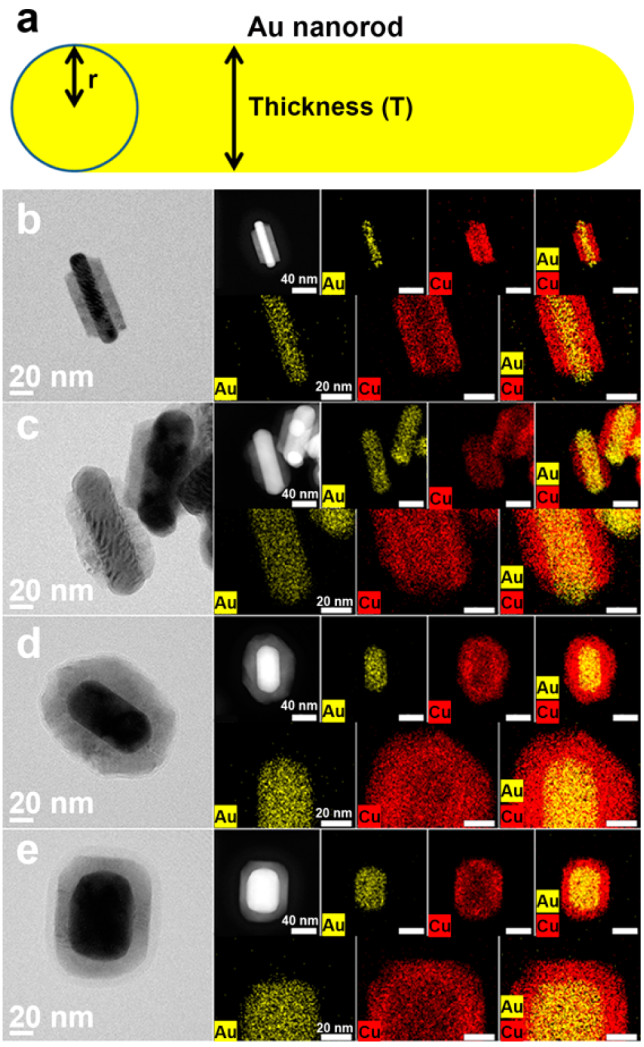

Figure 5. (a) Structural model of an Au nanorod. TEM, HAADF-STEM, and corresponding HAADF-STEM-EDS elemental mapping images of HNCs obtained using Au nanorods with curvatures of (b) 0.13, (c) 0.067, (d) 0.053, and (e) 0.035 nm^{-1}.

nanorod tip is assumed to be a hemisphere of which diameter ($2r$) is same with the thickness of Au nanorod, T (Figure 5a). The curvatures of the Au nanorod tips, κ, were then calculated by the following equation: $\kappa = 2/T\ (= 1/r)$. Notably, as in the case of the $Au_{vertex\text{-}exp}$−Cu_2O HNCs, tip-exposed Au nanorod−Cu_2O HNCs were obtained by using Au nanorods with curvatures higher than 0.06 nm^{-1}, whereas Au nanorods with curvatures of 0.053 and 0.035 nm^{-1} yielded Au nanorod@Cu_2O core−shell HNCs (Figure 5b−e). Apparently, these results further indicate that the high-curvature sites of Au NCs can facilitate the adsorption of the CTAB/SDS binary stabilizer and hence are deprived of Cu_2O deposition. Taken together, our findings show that the selective stabilization of Au NC

DOI: 10.1021/jacs.6b10288
J. Am. Chem. Soc. 2016, 138, 15766−15773

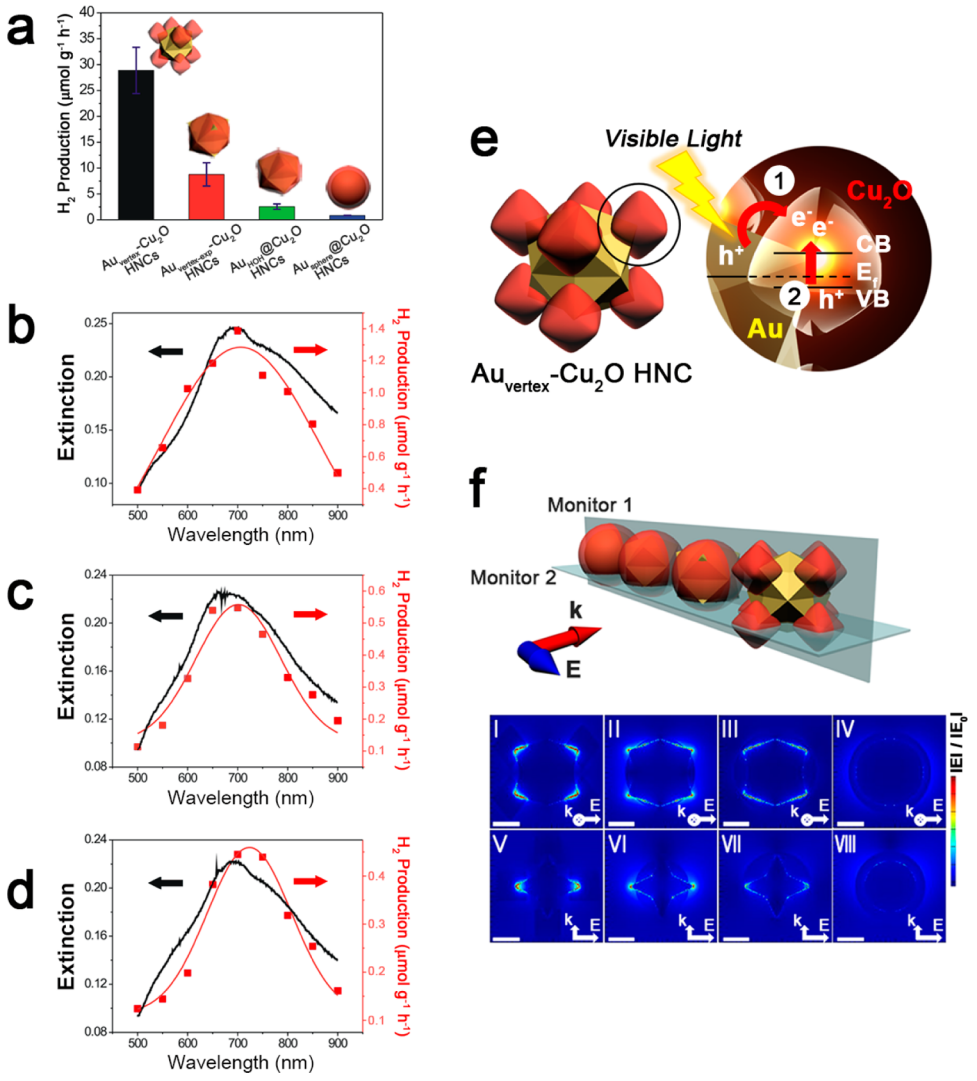

Figure 6. (a) Photocatalytic hydrogen generation rates of different HNCs. Action spectra obtained with Au_{vertex}–Cu_2O (b), $Au_{vertex\text{-}exp}$–Cu_2O (c), and Au_{HOH}@Cu_2O HNCs (d). (e) Schematic illustration of possible plasmon-induced charge separation processes for Au_{vertex}–Cu_2O HNCs (1: HET, 2: EMT). (f) FDTD-simulation models for calculating |*E*| distributions of HNCs and |*E*| distributions of Au_{vertex}–Cu_2O (I,V), $Au_{vertex\text{-}exp}$–Cu_2O (II,VI), Au_{HOH}@Cu_2O (III,VII), and Au_{sphere}@Cu_2O HNCs (IV,VIII) shown for monitor 1 (I–IV) and monitor 2 planes (V–VIII) with λ_{ex} of 700 nm. The scale bars in I–VIII indicate 50 nm.

surfaces with the aid of pertinent stabilizers can allow fine control over the structure of HNCs.

Plasmonic Photocatalysis with HNCs. To elucidate the relationship between the solar energy conversion efficiency and the topology of the HNCs, the photocatalytic hydrogen production properties of the HNCs were investigated in an aqueous solution containing methanol as a hole scavenger under visible-light irradiation (λ > 400 nm) with a 300 W Xe lamp (power density = 100 mW cm^{-2}, the lamp emission spectrum is shown in Figure S6). See the Supporting Information for experimental details. For comparison, the photocatalytic activities of spherical Au NC@Cu_2O core–shell HNCs (Au_{sphere}@Cu_2O HNCs), Cu_2O NCs, HOH Au NCs, and a physical mixture of Cu_2O and HOH Au NCs were also examined. The Au_{sphere}@Cu_2O HNCs were prepared by using spherical Au NC seeds with an average size similar to that of the HOH Au NCs (130 nm) (Figure S7), and the Cu_2O NCs were synthesized by slight modification of the reported procedure (Figure S8).[34] Notably, the photocatalytic activity of the HNCs highly depended on their coupling manner as well as the shape of the plasmonic NC domain. Indeed, the Au_{vertex}–Cu_2O HNCs formed by the selective overgrowth of Cu_2O on multiple high-curvature sites of the HOH Au NCs, the vertices$_{<111>}$, exhibited outstanding photocatalytic activity for hydrogen production relative to the other HNCs, of which the hydrogen generation rate was 28.87 μmol g^{-1} h^{-1} (Figure 6a). The hydrogen production activities of the $Au_{vertex\text{-}exp}$–Cu_2O, Au_{HOH}@Cu_2O, and Au_{sphere}@Cu_2O HNCs were 8.80, 2.55, and 0.87 μmol g^{-1} h^{-1}, respectively (Figure 6a). On the contrary, the pure Cu_2O NCs and the physical mixture of Cu_2O NCs + HOH Au NCs showed markedly inferior activity as compared to that of the HNCs; the hydrogen generation rates of the Cu_2O NCs and the physical mixture of Cu_2O NCs + HOH Au NCs were 0.22 and 0.08 μmol g^{-1} h^{-1}, respectively. Hydrogen production was not detected with the pure HOH Au NCs or in the absence of catalysts. Evidently, the superb photocatalytic activity of the HNCs compared to the pure Cu_2O NCs corroborates the promotional effect of plasmonic Au NCs on the photocatalytic function of Cu_2O. In addition, the low photocatalytic activity of the physical mixture of Cu_2O NCs +

DOI: 10.1021/jacs.6b10288
J. Am. Chem. Soc. 2016, 138, 15766–15773

HOH Au NCs substantiates the importance of intimate coupling between plasmonic metal and semiconductor. Notably, each action spectrum of the Au_{vertex}−Cu_2O, $Au_{vertex\text{-}exp}$−Cu_2O, and Au_{HOH}@Cu_2O HNCs collected under monochromatic light irradiation shows a fairly close correlation between the photocatalytic activity and the extinction spectrum of the HNCs, of which the spectral features are dominated by the SPR profile of the HOH Au NCs (Figures 6b−d and S9), thereby suggesting that the promotional effect of the Au NCs is indeed due to their plasmon excitation.[1,35] The temperature variations of the reaction mixtures versus irradiation time for all the catalysts tested showed very similar changes in temperature (Figure S10). Together with the lack of photocatalytic activity for the pure HOH Au NCs, this implies that the effect of plasmonic heating on photocatalysis is negligible. A recyclability test with the Au_{vertex}−Cu_2O HNCs for photocatalytic hydrogen production further demonstrated that the prepared HNCs can be used as recyclable visible-light photocatalysts in hydrogen production (Figure S11).

Mechanistic Studies on Plasmonic Photocatalysis with HNCs. The proposed approach, which enables the site-selective overgrowth of Cu_2O on desired sites of HOH Au NCs, can provide an opportunity to precisely explore plasmon-induced photocatalytic performance in terms of the structure of plasmonic metal−semiconductor HNCs and to obtain mechanistic insights into plasmon-mediated photocatalysis. As previously mentioned, the enhanced solar energy conversion efficiency of plasmonic metal−semiconductor HNCs can be attributed to an accelerated charge carrier generation rate in the semiconductor due to the transfer of the plasmon energy of the metal to the semiconductor through the HET or EMT process, or both. These possible plasmon-induced charge separation processes for Au_{vertex}−Cu_2O HNCs are schematically shown in Figure 6e (1: HET, 2: EMT). The electrons populated in the CB of Cu_2O then lead to the reduction of H_2O to produce hydrogen. In this context, the higher photocatalytic activities of HNCs containing the HOH Au NCs relative to Au_{sphere}@Cu_2O HNCs can easily be understood, as the sharp surface features of HOH Au NCs can provoke enormous plasmon excitation compared to spherical Au NCs. However, in our experiments, Au_{vertex}−Cu_2O, $Au_{vertex\text{-}exp}$−Cu_2O, and Au_{HOH}@Cu_2O HNCs showed markedly different photocatalytic activities, although they were constructed by using identical HOH Au NCs as seeds. This implies that the growth mode of Cu_2O on HOH Au NCs has a profound influence on the characteristics of plasmon energy transfer in HNCs.

To verify the effect of the plasmonic characteristics of HNCs on their photocatalytic function, the EM field enhancement around HNCs was analyzed using the FDTD method. Figure 6f shows the FDTD-simulated EM field amplitude ($|E|/|E_0|$) distributions around HNCs with the excitation wavelength (λ_{ex}) of 700 nm. The λ_{ex} was chosen based on the extinction and action spectra of the HNCs, at which the HNCs showed maximum extinction and photocatalytic activity (Figures 6b−d and S9a). The refractive index of the surrounding water (1.33) was taken into account as a dielectric medium. The geometric models of the HNCs were constructed based on their experimentally obtained structural parameters. Apparently, much stronger EM field enhancements are indeed localized at the high-curvature sites of the Au_{vertex}−Cu_2O (15.3-fold), $Au_{vertex\text{-}exp}$−Cu_2O (10.3-fold), and Au_{HOH}@Cu_2O HNC (9.7-fold) relative to the Au_{sphere}@Cu_2O HNC. It is worth highlighting that the Au_{vertex}−Cu_2O HNC showed highly enhanced localization of the EM field at their vertices$_{<111>}$ as compared to the other HNCs containing HOH Au NCs. An identical trend was observed with λ_{ex} values of 750 and 800 nm (Figure S12). The significant EM field enhancement of the Au_{vertex}−Cu_2O HNCs may be due to the fact that both Cu_2O and water with drastically different refractive indexes (refractive index of Cu_2O at 700 nm = 2.88)[36] surround the vertices$_{<111>}$ regions of HOH Au NCs, which can induce the preferential formation of a strong EM field at the interface between Au and Cu_2O.[16] The enhanced plasmon excitation of Au_{vertex}−Cu_2O HNCs due to their specific configuration can thus lead to much higher photocatalytic activity compared to that of $Au_{vertex\text{-}exp}$−Cu_2O and Au_{HOH}@Cu_2O HNCs. Interestingly, although the $Au_{vertex\text{-}exp}$−Cu_2O HNCs exhibited a plasmon excitation similar to that of the Au_{HOH}@Cu_2O HNCs, and their Cu_2O domain could not fully exploit the strong EM field localized at the vertices$_{<111>}$, they showed 3.5-fold higher photocatalytic activity relative to the Au_{HOH}@Cu_2O HNCs. This suggests that the contribution of the HET mechanism to plasmon-enhanced photocatalysis is dominant for Au−Cu_2O HNCs, rather than that of the EMT mechanism. Given that restoring charge balance to plasmonic metal in HNCs by the scavenging of accumulated holes is indispensable for a sustainable HET process,[4,7] the continuous transfer of plasmon-induced hot electrons in Au to Cu_2O can be expedited for Au_{vertex}−Cu_2O and $Au_{vertex\text{-}exp}$−Cu_2O HNCs due to their exposed Au surfaces, on which the oxidation of hole scavengers (methanol) can occur, resulting in the enhanced photocatalytic activity. On the contrary, Au_{HOH}@Cu_2O HNCs are deprived of the accessibility of their Au surfaces to hole scavengers owing to the complete Cu_2O shell; hence, only the inefficient EMT process is available for the plasmon energy transfer.

To confirm the proposed mechanism of the plasmon-induced photocatalysis, thin insulating SiO_2 layers were embedded between the Au and Cu_2O domains of the Au_{vertex}−Cu_2O and Au_{HOH}@Cu_2O HNCs, and the photocatalytic hydrogen production efficiencies of the resultant HNCs were compared with those of the pristine HNCs. The HNCs containing an intervening SiO_2 layer were synthesized using Au_{HOH}@SiO_2 core−shell NCs comprising HOH Au NC cores surrounded by 1−2 nm SiO_2 shells as seeds (Figure S13). HAADF-STEM images and corresponding EDS elemental analysis data of the prepared samples demonstrate the successful formation of SiO_2-embedded HNCs, Au_{HOH}@$SiO_{2\text{-}vertex}$−Cu_2O and Au_{HOH}@SiO_2@Cu_2O HNCs (Figure 7a−f). The presence of a 1−2 nm SiO_2 layer in the HNCs was clearly indicated by the presence of dark contrast between the Au and Cu_2O domains in the high-magnification HAADF-STEM images (denoted by arrows in Figure 7c,f). As insulating SiO_2 layers in the SiO_2-embedded HNCs can effectively prevent the injection of photogenerated hot electrons from Au into Cu_2O whereas EM field-mediated plasmon energy transfer is not significantly deteriorated due to their small thickness,[11,37] a comparison of the photocatalytic activity of SiO_2-embedded HNCs with that of pristine HNCs can provide important insights into the operating mechanism of plasmon-induced photocatalysis. In fact, FDTD-simulated EM field enhancement around the SiO_2-embedded HNCs was very similar to that of the pristine HNCs (Figure 7g). Interestingly, the Au_{HOH}@$SiO_{2\text{-}vertex}$−Cu_2O HNCs exhibited a remarkable decrease (8.1-fold) in photocatalytic activity for hydrogen production (3.58 μmol g^{-1} h^{-1}) compared to the Au_{vertex}−Cu_2O HNCs, whereas the Au_{HOH}@SiO_2@Cu_2O HNCs

DOI: 10.1021/jacs.6b10288
J. Am. Chem. Soc. 2016, 138, 15766−15773

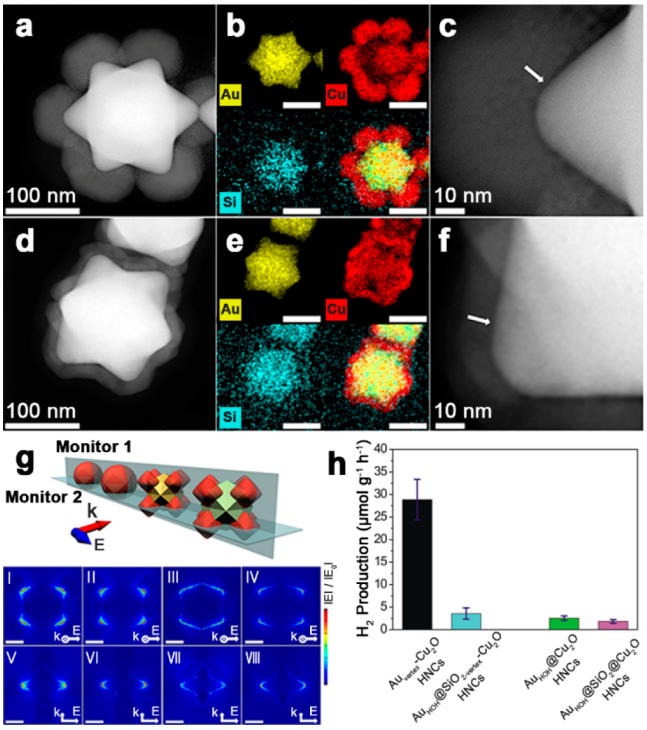

Figure 7. HAADF-STEM (a and d), corresponding HAADF-STEM-EDS elemental mapping (b and e), and high-magnification HAADF-STEM images (c and f) of $Au_{HOH}@SiO_{2\text{-vertex}}–Cu_2O$ (a–c) and $Au_{HOH}@SiO_2@Cu_2O$ HNCs (d–f). The scale bars in b and e indicate 100 nm. (g) FDTD-simulation models for calculating $|E|$ distributions of SiO_2-embedded HNCs and $|E|$ distributions of $Au_{HOH}@SiO_{2\text{-vertex}}–Cu_2O$ (I,V), $Au_{vertex}–Cu_2O$ (II,VI), $Au_{HOH}@SiO_2@Cu_2O$ (III,VII), and $Au_{HOH}@Cu_2O$ HNCs (IV,VIII) shown for monitor 1 (I–IV) and monitor 2 planes (V–VIII) with λ_{ex} of 700 nm. The scale bars in I–VIII indicate 50 nm. (h) Photocatalytic hydrogen generation rates of SiO_2-embedded HNCs and corresponding pristine HNCs.

showed photocatalytic activity (1.83 μmol g^{-1} h^{-1}) comparable to that of the $Au_{HOH}@Cu_2O$ HNCs (Figure 7h). Evidently, these results indicate that the HET process is the principal mechanism for the enhancement of the photocatalytic activity of Au–Cu_2O HNCs when continuous restoring charge balance is established, which is in line with the above inference.

Based on previous findings that the metal–support interface can promote catalytic performance by lowering activation energies for several catalytic reactions, such as CO oxidation, water–gas shift reaction, and electrocatalytic hydrogen evolution,[38−40] it can be suspected that the enhanced photocatalytic activity of the $Au_{vertex}–Cu_2O$ HNCs may be due to increased surface area of exposed Au–Cu_2O interface sites. However, in the case of photocatalytic hydrogen production reaction, photocatalytic activity is primarily dependent on processes within photocatalysts, such as photoexcitation, migration of charge carriers to the surface of photocatalysts, and charge recombination.[41,42] Accordingly, we believe that the superior photocatalytic activity of the $Au_{vertex}–Cu_2O$ HNCs is indeed associated with plasmonic effects rather than the effect of the Au–Cu_2O interface.

CONCLUSIONS

We have demonstrated a novel synthetic strategy for the site-selective overgrowth of semiconductor on desired sites of anisotropic plasmonic metal NCs to construct plasmonic metal–semiconductor HNCs with a desired coupling manner between constituents, which are not readily available otherwise. Both the highly anisotropic structural characteristics of plasmonic NCs imparted by high density of vertices with distinctively different curvatures and the proper use of a stabilizer are keys to the realization of HNCs with a specific configuration. HNCs produced by the selective overgrowth of Cu_2O on the multiple high-curvature sites of HOH Au NCs exhibited much more pronounced photocatalytic activity toward hydrogen production relative to that of other HNCs with different growth modes of Cu_2O due to efficient charge separation by strong plasmon excitation at the interface between Au and Cu_2O and subsequent sustainable HET. This emphasizes the importance of precise control over the architecture of HNCs in order to fully harness the plasmonic function of the metal NC domain in HNCs and, hence, to attain high solar energy conversion efficiency. We envision that this study could be extended to the fabrication of multi-component nanostructures with unprecedented topologies and functions and that it will pave the way to the development of a new class of solar energy conversion materials.

ASSOCIATED CONTENT

Supporting Information

The Supporting Information is available free of charge on the ACS Publications website at DOI: 10.1021/jacs.6b10288.

Experimental and calculation details and additional data (PDF)

AUTHOR INFORMATION

Corresponding Author

*sangwoohan@kaist.ac.kr

ORCID

Sang Woo Han: 0000-0001-5406-5211

Author Contributions

J.W.H. and D.H.W. contributed equally to this work.

Notes

The authors declare no competing financial interest.

ACKNOWLEDGMENTS

This work was supported by the Basic Science Research Program (2015R1A3A2033469) through the National Research Foundation of Korea (NRF) funded by the Ministry of Science, ICT & Future Planning (MSIP).

REFERENCES

(1) Mubeen, S.; Lee, J.; Singh, N.; Krämer, S.; Stucky, G. D.; Moskovits, M. *Nat. Nanotechnol.* **2013**, *8*, 247.

(2) Wang, C.; Astruc, D. *Chem. Soc. Rev.* **2014**, *43*, 7188.

(3) Li, J.; Cushing, S. K.; Zheng, P.; Senty, T.; Meng, F.; Bristow, A. D.; Manivannan, A.; Wu, N. *J. Am. Chem. Soc.* **2014**, *136*, 8438.

(4) Weng, L.; Zhang, H.; Govorov, A. O.; Ouyang, M. *Nat. Commun.* **2014**, *5*, 4792.

(5) Li, B.; Gu, T.; Ming, T.; Wang, J.; Wang, P.; Wang, J.; Yu, J. C. *ACS Nano* **2014**, *8*, 8152.

(6) Wu, K.; Chen, J.; McBride, J. R.; Lian, T. *Science* **2015**, *349*, 632.

(7) Huang, Z.; Liu, Y.; Zhang, Q.; Chang, X.; Li, A.; Deng, L.; Yi, C.; Yang, Y.; Khashab, N. M.; Gong, J.; Nie, Z. *Nat. Commun.* **2016**, *7*, 12147.

(8) Wu, B.; Liu, D.; Mubeen, S.; Chuong, T. T.; Moskovits, M.; Stucky, G. D. *J. Am. Chem. Soc.* **2016**, *138*, 1114.

(9) Linic, S.; Christopher, P.; Ingram, D. B. *Nat. Mater.* **2011**, *10*, 911.

DOI: 10.1021/jacs.6b10288
J. Am. Chem. Soc. 2016, 138, 15766–15773

(10) Liu, L.; Ouyang, S.; Ye, J. *Angew. Chem., Int. Ed.* **2013**, *52*, 6689.
(11) Cushing, S. K.; Li, J.; Meng, F.; Senty, T. R.; Suri, S.; Zhi, M.; Li, M.; Bristow, A. D.; Wu, N. *J. Am. Chem. Soc.* **2012**, *134*, 15033.
(12) Kelly, K. L.; Coronado, E.; Zhao, L. L.; Schatz, G. C. *J. Phys. Chem. B* **2003**, *107*, 668.
(13) Rodríguez-Lorenzo, L.; Álvarez-Puebla, R. A.; Pastoriza-Santos, I.; Mazzucco, S.; Stéphan, O.; Kociak, M.; Liz-Marzán, L. M.; García de Abajo, F. J. *J. Am. Chem. Soc.* **2009**, *131*, 4616.
(14) Yin, P.-G.; You, T.-T.; Tan, E.-Z.; Li, J.; Lang, X.-F.; Jiang, L.; Guo, L. *J. Phys. Chem. C* **2011**, *115*, 18061.
(15) Xia, X.; Zeng, J.; McDearmon, B.; Zheng, Y.; Li, Q.; Xia, Y. *Angew. Chem., Int. Ed.* **2011**, *50*, 12542.
(16) Seh, Z. W.; Liu, S.; Low, M.; Zhang, S.-Y.; Liu, Z.; Mlayah, A.; Han, M.-Y. *Adv. Mater.* **2012**, *24*, 2310.
(17) Lassiter, J. B.; Aizpurua, J.; Hernandez, L. I.; Brandl, D. W.; Romero, I.; Lal, S.; Hafner, J. H.; Nordlander, P.; Halas, N. J. *Nano Lett.* **2008**, *8*, 1212.
(18) Ghenuche, P.; Cherukulappurath, S.; Taminiau, T. H.; van Hulst, N. F.; Quidant, R. *Phys. Rev. Lett.* **2008**, *101*, 116805.
(19) Zhao, Q.; Ji, M.; Qian, H.; Dai, B.; Weng, L.; Gui, J.; Zhang, J.; Ouyang, M.; Zhu, H. *Adv. Mater.* **2014**, *26*, 1387.
(20) Simon, T.; Bouchonville, N.; Berr, M. J.; Vaneski, A.; Adrović, A.; Volbers, D.; Wyrwich, R.; Döblinger, M.; Susha, A. S.; Rogach, A. L.; Jäckel, F.; Stolarczyk, J. K.; Feldmann, J. *Nat. Mater.* **2014**, *13*, 1013.
(21) Rycenga, M.; Langille, M. R.; Personick, M. L.; Ozel, T.; Mirkin, C. A. *Nano Lett.* **2012**, *12*, 6218.
(22) Hong, J. W.; Lee, S.-U.; Lee, Y. W.; Han, S. W. *J. Am. Chem. Soc.* **2012**, *134*, 4565.
(23) Wang, W.-C.; Lyu, L.-M.; Huang, M. H. *Chem. Mater.* **2011**, *23*, 2677.
(24) Costi, R.; Saunders, A. E.; Banin, U. *Angew. Chem., Int. Ed.* **2010**, *49*, 4878.
(25) Puzder, A.; Williamson, A. J.; Zaitseva, N.; Galli, G.; Manna, L.; Alivisatos, A. P. *Nano Lett.* **2004**, *4*, 2361.
(26) Chen, H.; Shao, L.; Li, Q.; Wang, J. *Chem. Soc. Rev.* **2013**, *42*, 2679.
(27) Ye, X.; Gao, Y.; Chen, J.; Reifsnyder, D. C.; Zheng, C.; Murray, C. B. *Nano Lett.* **2013**, *13*, 2163.
(28) Zhang, J.; Langille, M. R.; Personick, M. L.; Zhang, K.; Li, S.; Mirkin, C. A. *J. Am. Chem. Soc.* **2010**, *132*, 14012.
(29) Kuo, C.-H.; Hua, T.-E.; Huang, M. H. *J. Am. Chem. Soc.* **2009**, *131*, 17871.
(30) Kong, L.; Chen, W.; Ma, D.; Yang, Y.; Liu, S.; Huang, S. *J. Mater. Chem.* **2012**, *22*, 719.
(31) Moon, S. Y.; Kusunose, T.; Sekino, T. *Mater. Lett.* **2009**, *63*, 2038.
(32) Chakraborty, H.; Sarkar, M. *Langmuir* **2004**, *20*, 3551.
(33) Zhao, N.; Qi, L. *Adv. Mater.* **2006**, *18*, 359.
(34) Bao, H.; Zhang, W.; Hua, Q.; Jiang, Z.; Yang, J.; Huang, W. *Angew. Chem., Int. Ed.* **2011**, *50*, 12294.
(35) Xiao, F.-X.; Zeng, Z.; Liu, B. *J. Am. Chem. Soc.* **2015**, *137*, 10735.
(36) Palik, E. D. *Handbook of Optical Constants of Solids II*; Academic Press: Boston, MA, 1998.
(37) Brown, M. D.; Suteewong, T.; Kumar, R. S. S.; D'Innocenzo, V.; Petrozza, A.; Lee, M. M.; Wiesner, U.; Snaith, H. J. *Nano Lett.* **2011**, *11*, 438.
(38) Saavedra, J.; Doan, H. A.; Pursell, C. J.; Grabow, L. C.; Chandler, B. D. *Science* **2014**, *345*, 1599.
(39) Rodriguez, J. A.; Ma, S.; Liu, P.; Hrbek, J.; Evans, J.; Pérez, M. *Science* **2007**, *318*, 1757.
(40) Subbaraman, R.; Tripkovic, D.; Strmcnik, D.; Chang, K.-C.; Uchimura, M.; Paulikas, A. P.; Stamenkovic, V.; Markovic, N. M. *Science* **2011**, *334*, 1256.
(41) Hisatomi, T.; Maeda, K.; Takanabe, K.; Kubota, J.; Domen, K. *J. Phys. Chem. C* **2009**, *113*, 21458.
(42) Hisatomi, T.; Takanabe, K.; Domen, K. *Catal. Lett.* **2015**, *145*, 95.

DOI: 10.1021/jacs.6b10288
J. Am. Chem. Soc. 2016, 138, 15766−15773